Performance of a Coupled Arctic Climate Model Compared to MOSAiC Observations and its Sensitivity to a Change in Snow Thermal Conductivity

Bachelorarbeit

Bachelor of Science im Studiengang Physik

an der

Technischen Universität Berlin
Fakultät II – Mathematik und Naturwissenschaften

und dem

Alfred-Wegener-Institut
Helmholtz-Zentrum für Polar- und Meeresforschung

Verfasserin: Leonie Röntgen

1. Gutachter: Prof. Dr. Thomas Möller
2. Gutachterin: Dr. Annette Rinke

Abgabe am: 28. Juli 2022

Hiermit erkläre ich, dass ich die vorliegende Arbeit selbstständig und eigenhändig sowie ohne unerlaubte fremde Hilfe und ausschließlich unter Verwendung der aufgeführten Quellen und Hilfsmittel angefertigt habe.

_____

Berlin, den 28. Juli 2022

Abstract

Climate models like the coupled Arctic atmosphere-ocean-sea ice model HIRHAM-NAOSIM are helpful to gain a deeper understanding of Arctic Amplification and interactions between atmosphere, ocean and sea ice. HIRHAM-NAOSIM is evaluated in Arctic winter compared to data from the MOSAiC expedition for February 2020. A warm surface temperature bias of more than $5\,°\mathrm{C}$ during clear-sky conditions is discussed in terms of modeled surface energy budget, clouds and atmospheric stability. HIRHAM-NAOSIM's control run underestimates the stable atmospheric stratification and has a positive bias in liquid water path and longwave radiation during observed clear-sky time periods. Though the positive longwave radiative bias outweighs the impact of a changed snow thermal conductivity and the positive temperature bias during radiatively clear state remains, a halved conductivity of $0.15\,\mathrm{Wm^{-1}K^{-1}}$ reduces the simulated surface temperature by up to $5\,°\mathrm{C}$ and causes a higher occurrence of stable atmospheric conditions.

Zusammenfassung

Der weltweite Klimawandel ist auf Grund der polaren Verstärkung in der Arktis (engl.: *Arctic Amplification*) durch vergleichsweise schnell steigende Temperaturen sichtbar. Für ein tieferes Verständnis der Wechselwirkungen zwischen Atmosphäre, Ozean und dem arktischen Meereis werden gekoppelte regionale Klimamodelle herangezogen. Das gekoppelte Atmosphäre-Ozean-Modell HIRHAM-NAOSIM wird im arktischen Winter für Februar 2020 anhand von Beobachtungsdaten der MOSAiC Expedition (09/2019–10/2020) evaluiert. Während der kälteren Zeitperioden wird eine Überschätzung der simulierten Oberflächentemperatur von mehr als $5\,°\mathrm{C}$ beobachtet. Diese wird in Bezug auf die Energiebilanz, Wolken und atmosphärische Stabilität des Modells diskutiert. Der Kontrolllauf von HIRHAM-NAOSIM unterschätzt das Auftreten von stabilen atmosphärischen Schichtungen ebenso, wie den Anteil abwärts gerichteter langwelliger Strahlung während Zeiträumen mit wolkenlosem Himmel. Die erhöhte Oberflächentemperatur durch die Überschätzung der langwelligen Strahlung kann nicht durch eine verringerte Wärmeleitfähigkeit des Schnees ausgeglichen werden. Der Temperaturunterschied zwischen Modell und Beobachtung während des 'radiatively clear state' bleibt bestehen. Trotzdem reduziert eine Halbierung der thermischen Leitfähigkeit auf $0.15\,\mathrm{Wm^{-1}K^{-1}}$ die simulierte Oberflächentemperatur und bewirkt eine verbesserte Wiedergabe stabiler Zustände.

Contents

List of Symbols

CRE	cloud radiative effect in $\mathrm{Wm^{-2}}$
c_i	sea ice fraction
ϵ	surface emissivity $\epsilon = 0.985$
g	gravitational acceleration at North Pole $g = 9.83\,\mathrm{ms^{-2}}$ [1]
H_c	conductive heat flux in $\mathrm{Wm^{-2}}$
H_l	latent heat flux in $\mathrm{Wm^{-2}}$
H_s	sensible heat flux in $\mathrm{Wm^{-2}}$
h_i	ice thickness in m
h_s	snow thickness in m
IWV	vertically integrated water vapour in $\mathrm{kgm^{-2}}$
k_i	ice thermal conductivity in $\mathrm{Wm^{-1}K^{-1}}$
k_s	snow thermal conductivity in $\mathrm{Wm^{-1}K^{-1}}$
LW_d	downward longwave radiation in $\mathrm{Wm^{-2}}$
LW_net	net longwave radiation in $\mathrm{Wm^{-2}}$
LW_u	upward longwave radiation in $\mathrm{Wm^{-2}}$
LWP	liquid water path in $\mathrm{gm^{-2}}$
Ri_B	bulk Richardson number
R_net	net radiative fluxes in $\mathrm{Wm^{-2}}$
SEB	surface energy budget in $\mathrm{Wm^{-2}}$
SLP	sea-level pressure in hPa
SW_d	downward shortwave radiation in $\mathrm{Wm^{-2}}$
SW_net	net shortwave radiation in $\mathrm{Wm^{-2}}$
σ	Stefan-Boltzmann constant $\sigma \approx 5.67 \times 10^{-8}\,\mathrm{Wm^{-2}K^{-4}}$ [2]
T_10m	air temperature at 10 m height in °C
T_b	ice-bottom temperature in °C
T_s	surface temperature in °C
Θ_v	virtual potential temperature in K
U	horizontal windspeed component in $\mathrm{ms^{-1}}$
V	horizontal windspeed component in $\mathrm{ms^{-1}}$
z	height in m

1 Introduction

Climate change can be observed worldwide. New temperature records and the more frequent occurrence of extreme weather events are just two of many observable effects [3]. Various feedback effects lead to a faster change of the Artic climate compared to the global mean, a process known as Artic Amplification [4]. The ice-albedo feedback is one of the drivers of Arctic Amplification. It describes the loss of snow-covered sea ice due to higher temperatures and the resulting decrease of the surface albedo because of the darker ocean surface. More longwave radiation is absorbed, the temperature rises, and the sea ice reduction is amplified [5]. In the last 20 years surface temperatures in the Arctic increased by more than twice the global mean [6]. Changes of the Arctic climate can hereby also impact mid-latitude weather events via large-scale circulation patterns such as e.g. the Arctic Oscillation [7]. Therefore a deeper understanding and better simulation of the changing Arctic system and its feedback mechanisms is of high interest.

One tool to investigate feedbacks are coupled climate models like the Arctic atmosphere-ocean-sea ice model HIRHAM-NAOSIM [8]. Previous studies have shown that the model has biases in reproducing the observed sea ice extent and near-surface air temperature in wintertime [8]. The positive temperature bias in Arctic wintertime is a common bias in Arctic climate models, reanalysis, and forecasts and is often resulting from an inaccurate representation of the surface energy budget [9]. It is challenging to simulate the atmospheric boundary layer and its stability over Arctic sea ice because of the various interactions between clouds, radiation and turbulence over an inhomogeneous surface cover [10].

The MOSAiC (**M**ultidisciplinary drifting **O**bservatory for the **S**tudy of **A**rctic **C**limate) expedition marks the biggest attempt of humankind to observe one complete Arctic seasonal cycle from September 2019 to October 2020. The collected data give the opportunity to evaluate climate models and gain a better understanding of the Arctic atmosphere, ocean, cryosphere and ecosystem and their interactions [11].

The objective of this bachelor thesis is the evaluation of HIRHAM-NAOSIM in Arctic wintertime compared to observational data from the MOSAiC expedition. In the following Chapter 2 an overview of the physical background of Arctic winter climate characteristics is given. Chapter 3 introduces the MOSAiC expedition, the used data and experimental setups as well as the Arctic climate model HIRHAM-NAOSIM. Five synoptic events are analyzed and the applied statistical methods are introduced. The HIRHAM-NAOSIM control run ($CTRL$) is evaluated compared to MOSAiC data in Section 4.1. Afterwards, the influence of a changed snow thermal conductivity in the model setup is examined in Section 4.2. This quantitiy has been shown to be a key parameter in sea ice models, i.e. by Urrego-Blanco et al. [12]. Finally the results are summarized and compared to previous findings in Chapter 5.

2 Physical Background

This chapter provides an overview of important characteristics of Arctic climate in winter which are most relevant for this thesis. It includes the surface energy budget and its interaction with clouds, the two Arctic winter states and atmospheric stability. Afterwards, information about the snow thermal conductivity is given.

2.1 Surface Energy Budget

The surface energy budget (hereafter referred to as SEB) consists of turbulent and radiative fluxes as indicated in Equation (2.1). It describes the energy transfer across a surface interface without energy storages and determines the net surface heat flux between the atmosphere and the ocean, ice or land [13, p.110]. Radiative and non-radiative fluxes are defined as positive when directed towards the surface and negative when directed away from the surface. A negative SEB means that there is an energy loss of the surface corresponding to cooling effects, whereas a positive SEB is equivalent to a gaining of energy and leads to surface warming.

$$SEB = R_{\mathrm{net}} + H_{\mathrm{s}} + H_{\mathrm{l}} + H_{\mathrm{c}} \qquad (2.1)$$

H_{s} refers to the sensible heat flux, H_{l} the latent heat flux and H_{c} the conductive heat flux from ocean to atmosphere through sea ice and snow. The non-radiative fluxes H_{s} and H_{l} differ from each other because H_{s} is the heat transport along a vertical temperature gradient and H_{l} is the heat flux associated with phase transitions.

The total amount of radiative fluxes R_{net} can be calculated as sum of the net longwave and shortwave radiations LW_{net} and SW_{net} [13, p.111]

$$R_{\mathrm{net}} = LW_{\mathrm{net}} + SW_{\mathrm{net}} = LW_{\mathrm{d}} - \epsilon\sigma T_{\mathrm{s}}^4 + SW_{\mathrm{d}}(1 - \alpha). \qquad (2.2)$$

SW_{d} is the incoming solar radiation and LW_{d} the longwave component of LW_{net}, which is directed towards the surface. Figure 2.1 gives an overview of these incoming and outgoing fluxes and the structure of typical surface conditions in the Artic. Incoming shortwave radiation, which reaches the surface, gets absorbed or transmitted through ponds. With the surface albedo α as the ratio of reflected and incoming solar radiation, $SW_{\mathrm{d}} \cdot \alpha$ is the reflected shortwave radiation. According to the Stefan-Boltzmann law, the outgoing longwave flux can be calculated with the formula $LW_{\mathrm{u}} = \epsilon\sigma T_{\mathrm{s}}^4$ with the surface emissivity ϵ, the Stefan-Boltzmann constant σ and the surface skin temperature T_{s} [2, p.159]. In Arctic winter the SEB can be calculated as in Equation (2.1) without the shortwave radiation term SW_{net} due to a lack of incoming solar radiation during polar night [13, p.112]. There are no energy-transporting phase transitions except rare sublimation events in winter because the surface is frozen and T_{s} below $0\,^{\circ}\mathrm{C}$. For this reason the latent heat flux does not need to be considered as well. H_{c} is small compared to the radiative fluxes and therefore is not included in the calculation of
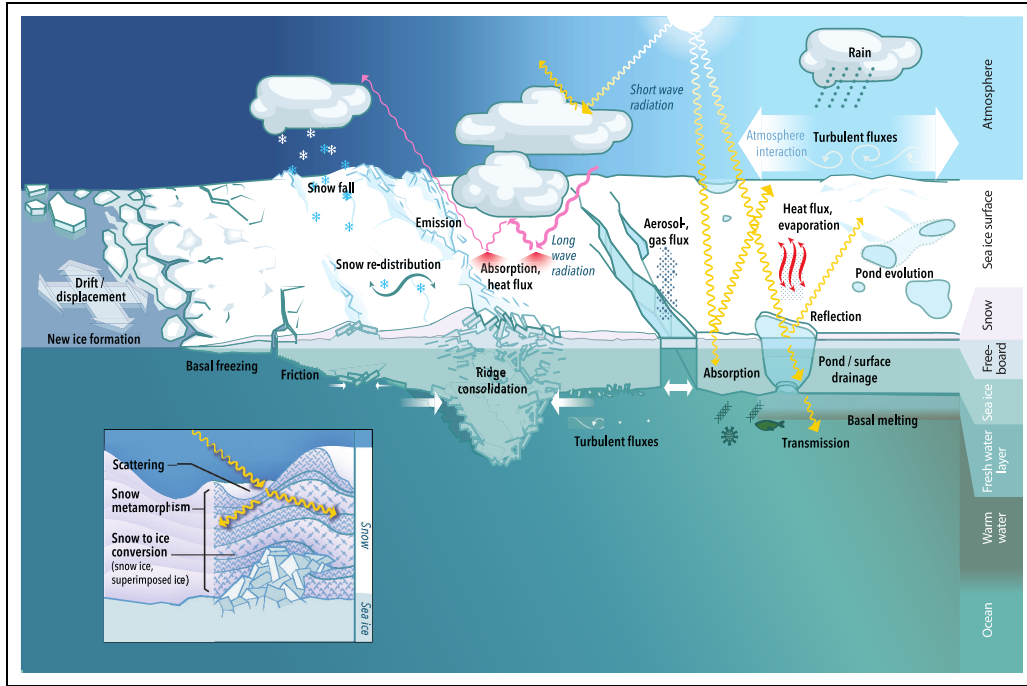
Figure 2.1: Schematic overview of incoming and outgoing radiative and non-radiative fluxes of the surface energy budget on sea ice. The ice is partly covered by snow and has some leads with direct contact between ocean and atmosphere. Incoming solar radiation SW_d is reflected due to the surface albedo. Longwave radiation is outgoing from the surface and incoming from the atmosphere (Stefan-Boltzmann). Moreover, sensible and latent turbulent heat fluxes above the surface affect the SEB. Through the ice and snow the conductive heat flux provides heat exchange between atmosphere and ocean. The graphic has been modified and is taken from [15].

SEB in Section 4.1. In spite of that, since changing the snow characteristics has an impact on the conductive heat fluxes, H_c is considered in Section 4.2.

The Arctic sea ice shown in Figure 2.1 separates the ocean from the atmosphere. Underneath the sea ice is a fresh water layer from basal melting situated above a layer of comparatively warm water. The edge of the sea ice can vary depending on thermodynamic and mechanical movements. Hereby, the dynamic of the sea ice can also lead to the formation of ridges and leads. Leads are open water areas within the sea ice cover, which quickly re-freeze with a thin ice layer in winter. They make an exchange of gases, aerosols and direct heat transfer from the warmer ocean to the atmosphere possible. Ridges cause momentum fluxes at the atmosphere-ice and ice-ocean interfaces. On parts of the sea ice there is a heterogeneous snow layer acting as insulator between sea ice and the atmosphere. The snows insulating effect plays an important role in the sea ice growth [14]. In the lower left of Figure 2.1 a more detailed picture of the snow ice interface is shown.

In addition to the sea ice characteristics, clouds have a big influence on the SEB as well. They affect the net shortwave radiation by reflecting the incoming solar radiation (albedo effect). By emitting thermal longwave radiation depending on their temperature they contribute to the net longwave radiation (greenhouse effect) [5]. Most of the time the downward LW radiation from the clouds results in warming. There is only a short

time period in Arctic summer when the shading of the clouds has a bigger impact than the greenhouse effects [16]. The Cloud Radiative Effect (CRE) is defined as the difference between the net radiative fluxes at cloud coverage and in clear-sky conditions. It quantifies the impact of clouds on the SEB. Shupe et al. [16] come to the conclusion that the CRE for longwave radiation mainly depends on the cloud temperature, height and cloud emissivity, whereas the shortwave CRE depends on the cloud shortwave radiation transmittance, surface albedo and the solar zenith angle. Clouds containing liquid water have a higher impact on the radiation budget than ice-only clouds [7]. For this, the liquid water path (LWP) is an important measure of the effect of clouds.

As a simplification, the Arctic winter climate can be separated into two states depending on the synoptic situation [17] [18]. These states are called 'radiatively clear state' and 'opaquely cloudy state'. They influence the atmosphere up to the stratosphere but are also impacting the ocean, sea ice and snow layers [18]. The radiatively clear state is characterised by calm periods [19]. Clouds during radiatively clear state are either too high above the surface to contribute to LW_net with downwelling longwave radiation or they have a too small optical thickness [18]. The small amount of LW_d leads to a net cooling effect. Synoptic situations with clear-sky condition are also typically characterized by higher sea-level pressures and lower windspeeds. The atmosphere is in a stable condition, which can last up to two weeks [18] and is characterized by a strong temperature inversion. Typical for the opaquely cloudy state are optically thick clouds consisting of liquid water. They occur during storms when heat and moisture is transported into the Arctic [17]. The presence of these clouds increases LW_d and therefore they contribute to a surface warming. Related winds to the stormy events decrease the atmospheric stability. As a result the temperature inversion becomes weaker [20]. The two Arctic winter states become visible in the bimodale structure in histogram plots of for example LW_net.

2.2 Atmospheric Stability

A measure of the atmospheric stability is the bulk Richardson number (Ri_B). It is based on the Monin–Obukhov similarity theory (MOST) [21] for near-surface turbulence [22]. In a stable stratified atmosphere turbulent fluxes counteract gravity. Higher windspeeds lead to an increase in turbulence, whereas a bigger buoyancy suppresses turbulence. Therefore Ri_B is calculated as quotient of the buoyancy and shear terms, and higher values of Ri_B are related to more stable stratification.

$$Ri_\text{B} = \frac{\frac{g}{\Theta_\text{v}} \Delta\Theta_\text{v} \Delta z}{\Delta U^2 + \Delta V^2} \tag{2.3}$$

The bulk Richardson number is calculated at $10\,\text{m}$ height. $g = 9.83\,\text{ms}^{-2}$ is the gravitational acceleration at the North Pole [1], Δz the depth of the considered atmospheric layer and ΔU and ΔV are horizontal changes of the windspeed components at $10\,\text{m}$. Equation (2.3) uses the virtual potential temperature Θ_v and $\Delta\Theta_\text{v}$, which is the vertical temperature gradient between $10\,\text{m}$ height and the surface.

Stable stratification is characterized by lower windspeeds and potentially a strong vertical temperature gradient. Since the windspeed is in the denominator of Equation (2.3) and the temperature gradient $\Delta\Theta_\text{v}$ in the numerator, Ri_B becomes higher in

more stable synoptic situations. Ri_B can be used to define three stability categories, namely unstable ($Ri_B < 0$), neutral ($0 \leq Ri_B < 0.02$) and stable ($0.02 \leq Ri_B$) [10, Supplementary Table 1].

2.3 Snow Thermal Conductivity

Snow has a relatively small thermal conductivity k_s compared to the thermal conductivity of sea ice k_i [9] and is the most reflective natural material on earth [23]. The thermal conductivity of ice depends on its salinity and temperature but a typical value for k_i of pure ice at $0\,°C$ is $2.24\,\mathrm{Wm^{-1}K^{-1}}$ [13, p.114]. For fresh snow k_s is in the order of $0.06\,\mathrm{Wm^{-1}K^{-1}}$, whereas k_s of older snow is in the order of $0.42\,\mathrm{Wm^{-1}K^{-1}}$ [13, p.114].

k_s is often estimated as function of the density of snow. But besides this, other parameters such as grain-size or snow temperature influence the thermal conductivity as well [24]. The fact that snow is also very heterogeneous [25] makes it difficult to measure or simulate its thermal conductivity. The calculation of the conductive heat flux H_c through ice and snow [26] includes the snow thermal conductivity.

$$H_c = \frac{c_i(T_b - T_s)}{h_i/k_i + h_s/k_s} \tag{2.4}$$

c_i is the sea ice fraction, T_s the surface temperature and T_b the ice-bottom temperature. h_i and h_s are ice and snow thicknesses and k_i and k_s are ice and snow thermal conductivities. A change of the thermal conductivity of snow leads to a changed amount of heat transfer from the ocean to the atmosphere and a resulting shift of the surface temperature and temperature gradient [27].

Several feedback effects have to be taken into account when evaluating the sensitivity of a climate model towards a change of the snow cover [13, p.144]. A smaller snow thermal conductivity for example increases the insulating effect of the snow layer causing a decrease of the heat loss towards the atmosphere. This leads to an inhibited basal ice growth [12] [14] [28]. High thermal conductivity has the opposite effect. A changed ice thickness influences the lead fraction and there are also feedback linkages to surface albedo and surface temperature [13] [29].

3 Data and Methods

This section introduces the observational data from the MOSAiC expedition and data from the regional coupled Arctic climate model HIRHAM-NAOSIM. In addition to that, the synoptic events of February 2020 and statistical methods are presented.

3.1 MOSAiC Expedition

3.1.1 MOSAiC Drift

The MOSAiC (**M**ultidisciplinary drifting **O**bservatory for the **S**tudy of **A**rctic **C**limate) expedition took about one year from September 2019 to October 2020 [30] and can be separated in five 'legs' as seen in Figure 3.1. The data used for this thesis originate from leg 2 and leg 3. Several observation stations were positioned around the RV Polarstern which was frozen into an ice floe using the Arctic ice drift to cross the Arctic ocean [31]. Aim of the expedition was to gather data from atmosphere, cyrosphere, ocean and ecosystem of a seasonal Arctic cycle and to enhance the understanding of their interactions to improve climate models and forecasts [11].

Figure 3.1: Overview of the MOSAiC expedition track. Legs of the MOSAiC expedition are distinguished by different colours with passive drift of the Polarstern as solid lines and active movement as dotted lines. The annual maximal and minimal sea ice edge from March 2020 and September 2019 is shown as well. Data used in this thesis are from leg 2 and leg 3. The figure is taken from [31].
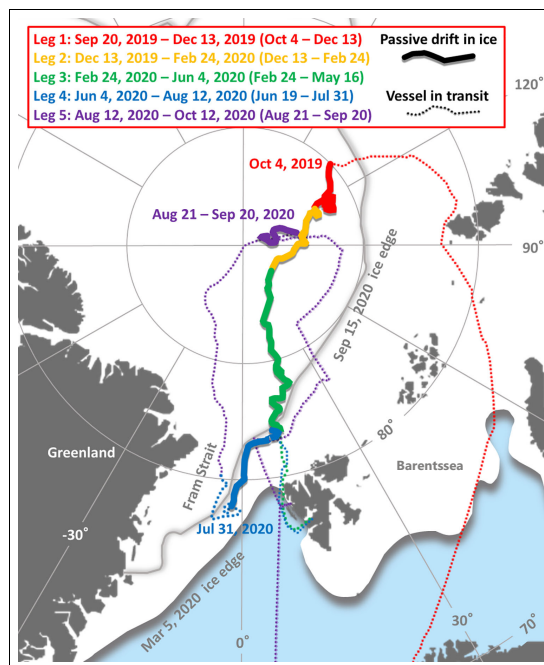
The Central Observatory (CO) including the Polarstern and instruments in a distance of 5 km was used to gain a detailed and interdisciplinary understanding of the Arctic seasonal cycle on a small scale. In addition to this, measurements took place in a distance of 5 km to 50 km around the CO in the Distributed Network (DN) to measure spatial variability and heterogenity [11].

3.1.2 Data

The data used in this thesis come from the meteorological site Met City installed in approximately 500 m distance to Polarstern and from three ASFS (autonomous Atmospheric Surface Flux Stations) situated in the Distributed Network in a distance of around 25 km to Polarstern. The tower at Met City is of 10 m height. Met City and station ASFS40 have data for the whole February 2020. For station ASFS30 data are available until 2020-02-27 and for station ASFS50 until 2020-02-06. Integrated water vapour (IWV) and liquid water path (LWP) are derived from a microwave radiometer onboard the Polarstern [32].

Table 3.1 lists the used MOSAiC variables which are relevant for SEB and their measurement instruments. Due to the early data version there is only unpublished information on systematical uncertainties. They are listed in Table 3.1 as well. The uncertainties of LWP and IWV depend on the elevation angle of the measurement and therefore are not itemized in Table 3.1. The data have a resolution of 1 min for temperatures and radiative fluxes and 10 min for the non-radiative fluxes. The resolution of LWP and IWV is between 1 s and 2 s. Each variable is averaged to three-hourly means if more than 50 % of data for the three hours is available. The threshold of 50 % data availability is set to avoid giving too much weight to outliers.

Table 3.1: MOSAiC's variables and measurement instruments at Met City, Polarstern and the ASFS stations. The locations, heights and abbreviations of the instruments are given [31]. Uncertainties are listed if the information is provided.

Variable	Location	Height in m	Instrument	Uncertainty
T_{10m}	Met City	9.34	Vaisala HMT330	$\pm 0.4\,°\mathrm{C}$
T_s	Met City	surface	PIR LW_u, LW_d	
	ASFS	surface	Apogee IRT; IR20 LW_u, LW_d	
LW_d	Met City	3.00	Eppley PIR	$\pm 2.6\,\mathrm{Wm^{-2}}$
	ASFS	2.00	Hukseflux IR20	$\pm 2.6\,\mathrm{Wm^{-2}}$
LW_u	Met City	1.50	Eppley PIR	$\pm 1.0\,\mathrm{Wm^{-2}}$
	ASFS	2.00	Hukseflux IR20	$\pm 1.0\,\mathrm{Wm^{-2}}$
H_s	Met City	2.00	Metek uSonic-Cage MP	
	ASFS	3.86	Metek uSonic-Cage MP	
U, V	Met City	10.54	Metek uSonic-Cage MP	$\pm 0.3\,\mathrm{ms^{-1}}$
IWV	Polarstern	29.00	RPG HATPRO G5	
LWP	Polarstern	29.00	RPG HATPRO G5	

The surface temperature T_s is derived from measurements of the longwave radiation parts LW_u and LW_d [33]

$$T_s = \left[\frac{LW_d - (1 - \epsilon)LW_u}{\epsilon\sigma} \right]^{0.25} . \tag{3.1}$$

$\epsilon = 0.985$ is the surface emissivity and $\sigma \approx 5.67 \times 10^{-8}\,\mathrm{Wm^{-2}K^{-4}}$ [2, p.159] the Stefan-Boltzmann constant.

3.2 Climate Model HIRHAM-NAOSIM

3.2.1 Model Description

The regional Arctic atmosphere-ocean-sea ice model couples the ocean-sea ice model NAOSIM (**N**orth **A**tlantic/**A**rctic **O**cean-**S**ea **I**ce **M**odel) [34] with the atmospheric model HIRHAM5 (**Hi**gh **R**esolution **Ham**burg) [35] [36]. The first version of this coupling was described 2003 [37] and the latest description is given in [8]. Further explanations of improvements in the parameterizations are made in [38] and [26].

The domains of HIRHAM5 and NAOSIM are depicted in Figure 3.2. The overlap area in which the stand-alone models are coupled is highlighted in yellow. HIRHAM5 has 40 vertical levels and a horizontal resolution of $0.25\,°$ ($\sim 25\,\mathrm{km}$) while NAOSIMs horizontal resolution is $1/12\,°$ ($\sim 9\,\mathrm{km}$) and it has 50 vertical levels [8].

Sea surface temperature, sea ice concentration, sea ice thickness, snow thickness on ice and the freezing temperature of sea water are transferred from NAOSIM to HIRHAM5 every hour in the coupled areas [8]. HIRHAM5 transfers the atmospheric fluxes to NAOSIM also with an hourly time interval. Responsible for the coupling is the software YAC 1.2.0 (**Y**et **A**nother **C**oupler) [8], [39]. In the small domain outside of the coupled area the models are treated as in stand-alone mode.

Figure 3.2: Domains of the stand-alone ocean model NAOSIM and atmosphere model HIRHAM5 in central Arctic. The area of the coupled model HIRHAM-NAOSIM is highlighted in yellow. The graphic is taken from [8].
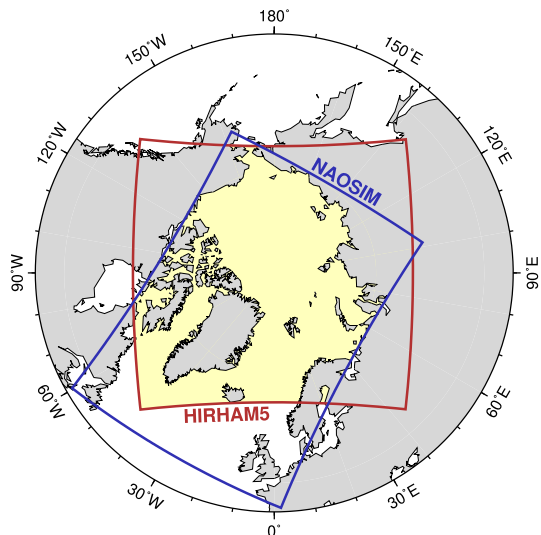
3.2.2 Model Experiments

The control run of HIRHAM-NAOSIM ($CTRL$) is simulated for the period from 2019-01-01 to 2020-05-01. It is started with the HN2.1 configuration and ice-ocean initialization from HN2.1 ensemble member 1 which is similar to the HN2.0 configuration described by Dorn et al. [8]. $CTRL$ is laterally driven with ERA5 reanalysis data [40] and nudged in all levels by $1\,\%$. Nudging describes the replacement of a percentage of the model data by reanalysis data [41].

As mentioned in Section 2.3 the thermal conductivity of snow depends, among other parameters, on the density of the snow and therefore varies a lot. Freshly fallen snow has a relatively small k_s and the estimated snow thermal conductivity of the MOSAiC expedition is $0.50\,\mathrm{Wm^{-1}K^{-1}}$ [42]. The choice of k_s and snow density influences the simulated sea ice volume [12]. The $CTRL$ run has a snow thermal conductivity of

$k_s = 0.31\,\mathrm{Wm^{-1}K^{-1}}$ like many other sea ice models [25]. To evaluate the impact of a change in k_s two sensitivity runs are carried out. In run $k15$ k_s is halved to $0.15\,\mathrm{Wm^{-1}K^{-1}}$, run $k50$ uses the estimated conductivity of MOSAiC. Table 3.2 gives an overview of the model runs and their snow thermal conductivities.

Table 3.2: HIRHAM-NAOSIM model runs, names and used snow thermal conductivities.

Model Run	Name	k_s in $\mathrm{Wm^{-1}K^{-1}}$
runN36_itd0	$CTRL$	0.31
runN36_itd0_consn_0.15	$k15$	0.15
runN36_itd0_consn_0.50	$k50$	0.50

3.3 Synoptic Events

Synoptic meteorology deals with the state of the atmosphere over a wide area including observations of the sky cover, atmospheric pressure and precipitation [43] [44]. The discussion is limited to February 2020. In this month, a variety of different meteorological conditions occurred. Clear-sky conditions as well as cases of warm air intrusions into the Arctic and storm events have been observed. They are discussed representative for the other months. Five time periods with specific events have been selected. The time periods are chosen based on the atmospheric circulation, namely integrated water vapour (IWV) and sea-level pressure (SLP) as well as the temperature difference between $CTRL$ run and MOSAiC observations.

Exemplary two of the synoptic situations are shown in Figure 3.3. In the days around 2020-02-19 12:00 a stormy event including a cyclone with its lowest pressure around $950\,\mathrm{hPa}$ is over the Barents-Kara Seas and influences the synoptic situation at Met City. During its passage south of Polarstern, SLP of $CTRL$ run at Met City decreases by approximately $20\,\mathrm{hPa}$ to $970\,\mathrm{hPa}$ and IWV rises by around $3\,\mathrm{kgm^{-2}}$ to values between $4\,\mathrm{kgm^{-2}}$ and $5\,\mathrm{kgm^{-2}}$ caused by the poleward transport of heat and moisture at the eastern flank of the cyclone. Another stormy event discussed takes place around 2020-02-03. A cyclone steers a moisture intrusion and pressure low from Barents Sea towards the Polarstern. This is shown in Figure 6.1 (left) appended to this thesis.

The plot on the left side of Figure 3.3 is from 2020-02-07 15:00. It shows a synoptic situation with pressures at around $1010\,\mathrm{hPa}$ and IWV around $1\,\mathrm{kgm^{-2}}$ to $2\,\mathrm{kgm^{-2}}$ at Met City. A similar synoptic situation with SLP between $1010\,\mathrm{hPa}$ and $1020\,\mathrm{hPa}$ and small values of IWV can be observed around 2020-02-10 and is depicted in the middle in Figure 6.1. Furthermore, the event around 2020-02-14 is taken into account. It was chosen because of the surface temperature difference of the $CTRL$ run and MOSAiC data, which was bigger than $5\,^\circ\mathrm{C}$ for over nine hours in a row. This event is characterized by a moisture intrusion from the Kara Sea and SLP at Polarstern is around $1000\,\mathrm{hPa}$. The Polarstern in Figure 6.1 (right) is on the edge of the moisture intrusion. This has to be considered when using only the nearest grid cell of HIRHAM-NAOSIM to Polarstern.
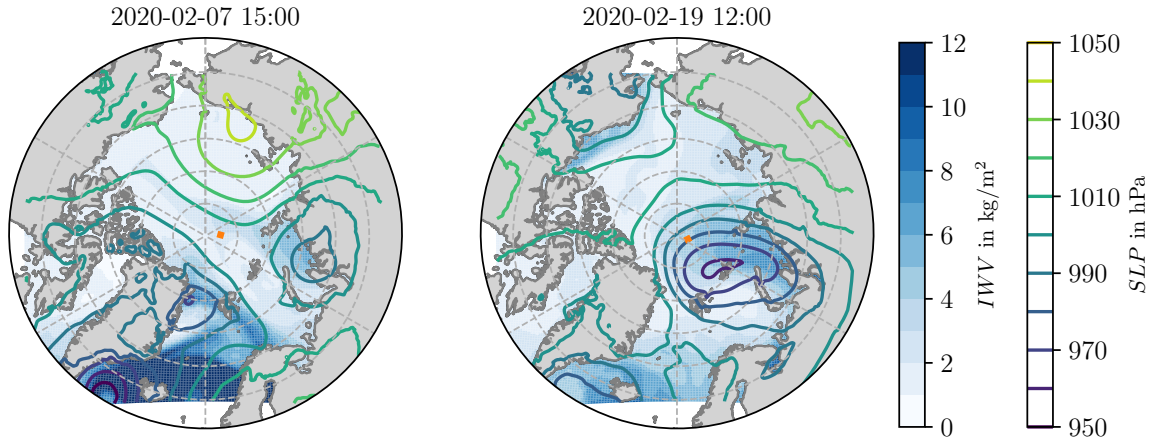
Figure 3.3: Spatial plots of integrated water vapour (IWV, shaded) and isobares of sea-level pressure (SLP) from HIRHAM-NAOSIM's control run ($CTRL$) in the Arctic at two times in February 2020. The position of Met City is marked in orange. The left plot from 2020-02-07 15:00 represents a synoptic situation with relatively high sea-level pressures at Polarstern and the plot on the right from 2020-02-19 12:00 shows the synoptic situation during a cyclone event over the Barents-Kara Seas.

3.4 Statistical Methods

The evaluation of the model in Chapter 4 uses MOSAiC data. Model output represents three-hourly grid cell averages, while the MOSAiC measurements are collected from four experimental sites. To compare the datasets, three-hourly means of the observational data are calculated and the nearest grid cell of HIRHAM-NAOSIM to each station is located for every time step of MOSAiC's drift using the function 'cKDTree' from scipy [45].

One method to compare observational and model data is time series analysis. It helps to connect synoptic events with model biases. In the discussion of Chapter 4 the MOSAiC data in the time series is plotted as the mean value of the stations. The standard deviation across the stations σ_{s} at each time step is calculated as

$$\sigma_{\mathrm{s}} = \sqrt{\frac{\sum_{s=1}^{n}(o_{\mathrm{s}} - \bar{o}_{\mathrm{s}})^2}{n}}. \tag{3.2}$$

It is also plotted for every time step. n is the number of stations with usable data with a maximum of four stations, o_{s} represents the data points of the different stations s and $\bar{o}_{\mathrm{s}}$ their mean value.

Furthermore, probability density function plots (pdf plots) are created to gain a better understanding of the distribution and range of the data. In contrast to histogram plots, the bins in the pdf plots are smoothed by a gaussian kernel. For plotting the pdfs in python seaborn's function 'kdeplot' [46] is used.

To evaluate the model quantitatively the mean bias error (MBE) is calculated as

the monthly mean difference of model and observational data with

$$MBE = \frac{1}{N} \sum_{i=1}^{N} (m_i - o_i).$$ (3.3)

o_i is the observational data and m_i are the values of the simulation belonging to the nearest grid cell to the station of o_i at time step i. N is the total number of time steps, which is 232 for February 2020 multiplied by the number of stations with available data.

Moreover, the root-mean-square error (RMSE) is taken into account with

$$RMSE = \sqrt{\frac{1}{N} \sum_{i=1}^{N} (m_i - o_i)^2}.$$ (3.4)

To perform a correlation analysis, the normalized covariance matrix M is calculated using numpy's function 'corrcoef' [47]. M of two datasets is calculated as their covariance matrix normalized by the product of their standard deviations [48]. The correlation ($corr$) of observational data o and model data m with their mean values $\bar{o}$ and $\bar{m}$ and standard deviations σ_m and σ_o is on the main diagonal of M and can be calculated as

$$corr = \frac{\frac{1}{N} \sum_{i=1}^{N} (o_i - \bar{o})(m_i - \bar{m})}{\sigma_m \sigma_o}.$$ (3.5)

4 Results and Discussion

This chapter first discusses the evaluation of the HIRHAM-NAOSIM control run ($CTRL$) compared to data from the MOSAiC expedition. Afterwards, the sensitivity of HIRHAM-NAOSIM to a change in snow thermal conductivity is examined.

4.1 Evaluation of the Control Run with MOSAiC Observations

Before going into details of temperature (Section 4.1.1), radiation (Section 4.1.2) and atmospheric stability (Section 4.1.3) an overview in Table 4.1 shows the model biases in temperature, SEB components, integrated water vapour (IWV) and liquid water path (LWP). The table contains the monthly mean of the observational data, mean bias errors and correlations.

Table 4.1: Variables for three-hourly MOSAiC and HIRHAM-NAOSIM data from February 2020 at Polarstern. The monthly mean value of MOSAiC data is derived from data of all stations. Mean bias error (MBE) and correlation ($corr$) are calculated using Equations (3.3) and (3.5) for three model runs with different snow thermal conductivities (k_s). The control run ($CTRL$) has a k_s of $0.31\,\mathrm{Wm^{-1}K^{-1}}$ and the thermal conductivies of the runs $k15$ and $k50$ are $0.15\,\mathrm{Wm^{-1}K^{-1}}$ and $0.50\,\mathrm{Wm^{-1}K^{-1}}$. Temperature, SEB components, IWV, and LWP are taken into account. From the surface upward directed fluxes are defined negative and downward directed fluxes positive.

Variable	MOSAiC mean	$CTRL$ MBE	$corr$	$k15$ MBE	$corr$	$k50$ MBE	$corr$
T_s	$-27.75\,°\mathrm{C}$	$2.13\,\mathrm{K}$	0.89	$1.27\,\mathrm{K}$	0.89	$2.56\,\mathrm{K}$	0.90
$T_\mathrm{10m}-T_\mathrm{s}$	$1.03\,\mathrm{K}$	$-0.19\,\mathrm{K}$	0.49	$0.05\,\mathrm{K}$	0.48	$-0.32\,\mathrm{K}$	0.50
H_s	$3.45\,\mathrm{Wm^{-2}}$	$8.26\,\mathrm{Wm^{-2}}$	0.30	$10.40\,\mathrm{Wm^{-2}}$	0.26	$6.96\,\mathrm{Wm^{-2}}$	0.32
LW_d	$173.09\,\mathrm{Wm^{-2}}$	$15.97\,\mathrm{Wm^{-2}}$	0.77	$14.67\,\mathrm{Wm^{-2}}$	0.77	$16.76\,\mathrm{Wm^{-2}}$	0.79
LW_u	$-206.18\,\mathrm{Wm^{-2}}$	$-7.96\,\mathrm{Wm^{-2}}$	0.86	$-5.07\,\mathrm{Wm^{-2}}$	0.86	$-9.39\,\mathrm{Wm^{-2}}$	0.87
LW_net	$-33.43\,\mathrm{Wm^{-2}}$	$9.02\,\mathrm{Wm^{-2}}$	0.56	$10.47\,\mathrm{Wm^{-2}}$	0.58	$8.41\,\mathrm{Wm^{-2}}$	0.59
SEB	$-29.19\,\mathrm{Wm^{-2}}$	$16.58\,\mathrm{Wm^{-2}}$	0.61	$20.54\,\mathrm{Wm^{-2}}$	0.59	$14.46\,\mathrm{Wm^{-2}}$	0.61
LWP	$3.62\,\mathrm{g\,m^{-2}}$	$2.66\,\mathrm{g\,m^{-2}}$	0.36	$2.59\,\mathrm{g\,m^{-2}}$	0.36	$2.66\,\mathrm{g\,m^{-2}}$	0.34
IWV	$2.92\,\mathrm{kg\,m^{-2}}$	$-0.55\,\mathrm{kg\,m^{-2}}$	0.92	$-0.56\,\mathrm{kg\,m^{-2}}$	0.92	$-0.55\,\mathrm{kg\,m^{-2}}$	0.92

All variables except LW_u, ΔT, and IWV have a positive bias in the mean February MBE for the control run. In the following sections, reference will be made to the contents of Table 4.1.

4.1.1 Temperature

The time series of three-hourly data from February 2020 for the surface temperature T_s is depicted in Figure 4.1. The observed temperature varies between $-40.37\,°C$ and $-10.62\,°C$. It reaches February's highest observed temperature during the cyclone event around 2020-02-19. The surface temperature decreases the most in the end of February.
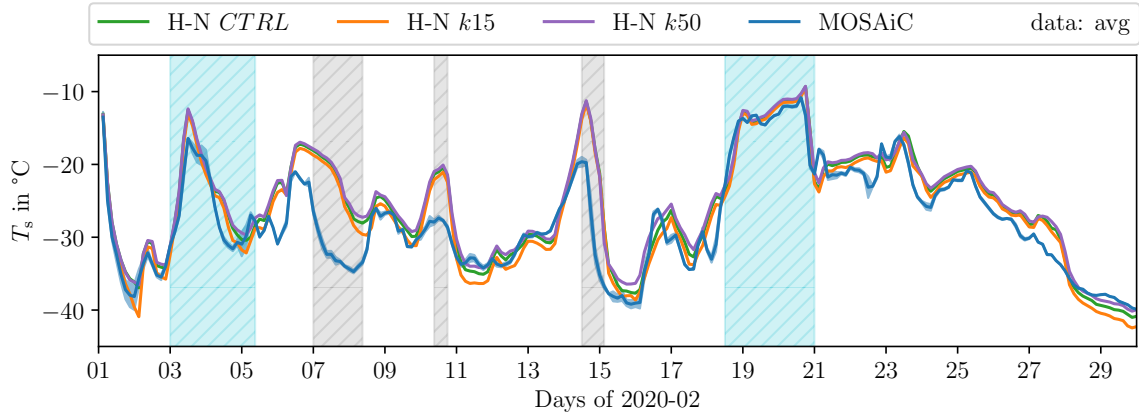

Figure 4.1: Time series of three-hourly surface temperature T_s for February 2020 at Polarstern. MOSAiC data are plotted as mean from Met City and the flux stations with the across station standard deviation σ in blue. σ of T_s is small. Model runs of HIRHAM-NAOSIM are averaged over the nearest grid cells to MOSAiC stations in green (control run $CTRL$), orange ($k15$) and purple ($k50$). For further evaluations some periods of time are hatched in blue and grey depending on the synoptic events described in Section 3.3.

To examine it more closely for the specific events presented in Section 3.3, there are blue and grey hatched periods in Figure 4.1. During the first cyclone event around 2020-02-03, the observed temperature rises from approximately $-35\,°C$ to $-17\,°C$. After a fast increase, the temperature drops again after the cyclone passage to around $-32\,°C$ on 2020-02-05. A similar strong temperature rise of approximately $19\,°C$ from $-32\,°C$ to $-13\,°C$ is observed during a cyclone event around 2020-02-19. T_s stays at around $-10\,°C$ until it decreases again when the cyclone has passed on 2020-02-20.

In the grey hatched periods, the MOSAiC surface temperature T_s decreases in the first and the third of the time periods at 2020-02-07 and around 2020-02-14. The decrease is particularly pronounced around 2020-02-07, when T_s drops from $-23\,°C$ to $-35\,°C$ in approximately one day. During the grey period around 2020-02-10 the temperature reaches a maximum followed by a decrease of approximately $5\,°C$ at the end of the day and the beginning of 2020-02-11.

The model is able to simulate the monthly temperature maximum and minimum of MOSAiC's observations. The temperature minimum of $CTRL$ ($-41.01\,°C$) and the maximum ($-9.31\,°C$) are close to the observed values and of similar timing. $CRTL$ matches the temporal changes in temperature with a correlation of 0.89 (Table 4.1) and a $RMSE$ of 2.75 K. The monthly MBE has a positive bias of 2.13 K, but the time series show that the temperature is not systematically overestimated in the model. Instead, in specific periods (grey hatched in Figure 4.1) the model is too warm.

Indeed, the surface temperature of $CTRL$ during stormy events in the blue hatched

19

periods rises as strong as the observed temperature. Especially in the second event around 2020-02-19 the modeled temperature is within the across station standard deviation and thus reproduces the observed T_s. The temperature increase of $CTRL$ run in the first blue time period is overestimated by approximately $3\,°\mathrm{C}$ compared to observations. Grey hatched periods are at times when the $CTRL$ surface temperature is more than $5\,°\mathrm{C}$ higher than the MOSAiC temperature for longer than nine hours in a row. This happens during synoptic events with observed temperatures beneath $-20\,°\mathrm{C}$ and clear-sky conditions. The model reproduces the temperature increase shortly before these cold periods but $CTRL$ remains at too high temperatures. In the third grey time period around 2020-02-14, $CTRL$ temperature rises as high as during the blue hatched times due to the modeled stormy intrusion nearby the grid cell of Polarstern.

The monthly positive bias of $CTRL$ run is visible in Figure 4.2. Maximum and minimum of the observed T_s are reached but the graph of $CTRL$ run is slightly shifted towards higher temperatures. The density of T_s is underestimated at low temperatures in the range of approximately $-40\,°\mathrm{C}$ to $-28\,°\mathrm{C}$ and overestimated for relatively warm temperature conditions within the range of $-25\,°\mathrm{C}$ to $-10\,°\mathrm{C}$.

Figure 4.2: Plot of the pdf of surface temperature T_s for February 2020 at MOSAiC drift. MOSAiC data is plotted in blue and the model output in green ($CTRL$), orange ($k15$) and purple ($k50$) for HIRHAM-NAOSIM runs with different k_s. The plot is based on three-hourly data and derived from Met City and the ASFS and their nearest grid cells of HIRHAM-NAOSIM.
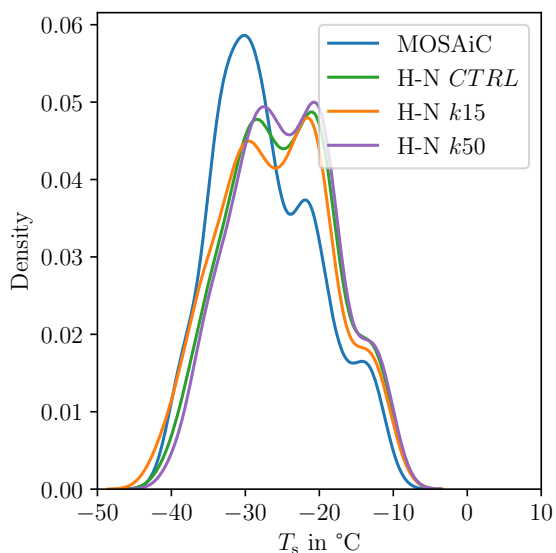
To conclude, the $CTRL$ run simulates the surface temperature with a high correlation of 0.89 compared to MOSAiC observations and there is no systematic over- or underestimation. Nevertheless, a positive temperature bias in synoptic situations with lower temperatures is observed. Three reasons to explain this positive bias are discussed in the following sections. One reason may be a positive bias in the downward longwave radiation (LW_d), the atmospheric stability is examined, and thirdly a change in snow thermal conductivity is evaluated regarding a possible reduction of the positive surface temperature bias [9].

4.1.2 Radiation and Clouds

A hypothesis explaining the positive temperature bias is a positive bias in LW_d resulting from, for example, a bias in clouds. The components of SEB and especially the

longwave downward radiation (LW_{d}) and liquid water path (LWP) from the $CTRL$ run are compared to MOSAiC data to verify this hypothesis.

Table 4.1 shows that the SEB and its components H_{s} and LW_{net} have monthly positive biases. The SEB has a MBE of $16.58\,\mathrm{Wm}^{-2}$ for the $CTRL$ run. The radiative fluxes LW_{u} and LW_{d} have relatively high correlations of > 0.7 compared to a low correlation of 0.33 for H_{s}. The correlation of SEB is 0.61 and $corr = 0.56$ for LW_{net}. The time series of LW_{net} and H_{s} as well as the one of the SEB are appended to the thesis in Figure 6.2. There are no obvious differences in the blue and grey hatched periods, which can be clearly interpreted as source of the positive temperature bias.

One important component of the longwave contribution to the SEB is LW_{d}. It directly depends on the presence of clouds [18]. This can be seen in Figure 4.3. Observed LW_{d} (left axis, solid) varies between $120\,\mathrm{Wm}^{-2}$ and $250\,\mathrm{Wm}^{-2}$ while the maximum of LWP (right axis, dotted) is at approximately $80\,\mathrm{gm}^{-2}$. The time series of MOSAiC's LW_{d} has maxima and minima at similar times as the measured surface temperature. Associated with the occurrence of storms (blue hatched periods and third grey period)
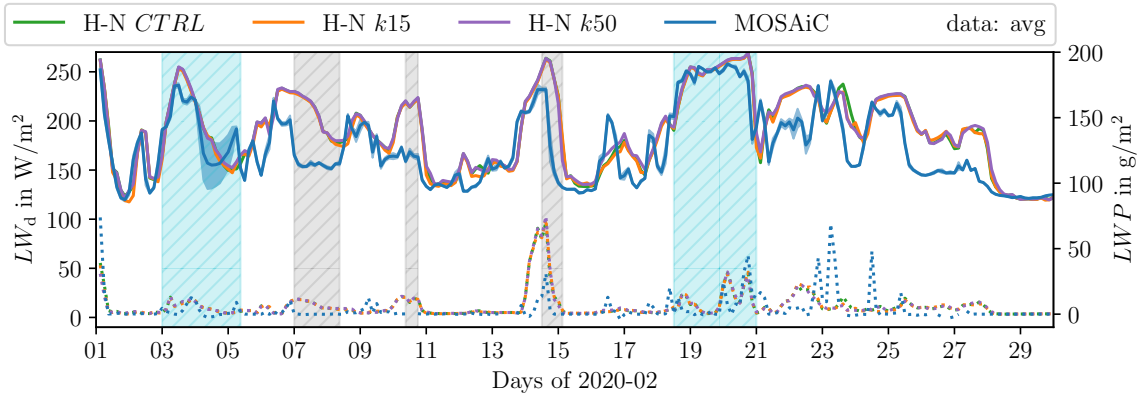

Figure 4.3: Time series of downward longwave radiation (solid line, left y-axis) and liquid water path (dotted, right y-axis) for February 2020. As in Figure 4.1 periods of time are hatched in different colours depending on temperature biases and synoptic situations. The data are three-hourly means at Met City and ASFS from MOSAiC observations with their across station standard deviation in blue and HIRHAM-NAOSIM runs in blue, orange and purple.

the observed LW_{d} and LWP increase and reach their highest values. Thus, clouds combined with a higher LWP (increase by $30\,\mathrm{gm}^{-2}$) contribute to an increased LW_{d} by $80\,\mathrm{Wm}^{-2}$ in the third grey period. During high-pressure situations in the two first grey periods, LWP shows values near $0\,\mathrm{gm}^{-2}$.

The $CTRL$ run has a positive monthly LWP bias of $2.66\,\mathrm{gm}^{-2}$ and a $RMSE$ of $6.33\,\mathrm{gm}^{-2}$ compared to MOSAiC (Table 4.1). The correlation of 0.36 is low, which indicates that some periods are in good agreement with the observations while others are not. Figure 4.3 shows a good LWP representation in the stormy time periods and the bias in LW_{d} in these time periods is relatively small (maximum only about $10\,\mathrm{Wm}^{-2}$ to $20\,\mathrm{Wm}^{-2}$) as well. A positive bias in LWP can be seen during the grey hatched periods. Related to the higher presence of cloud liquid water, the $CTRL$ run

also has a positive bias of LW_d (in the order of $40\,\mathrm{Wm^{-2}}$ to $80\,\mathrm{Wm^{-2}}$) in these time periods. The first two grey time periods are high-pressure situations associated with cold temperatures and clear sky. Figure 4.3 shows that the model in contradiction to the observation simulates liquid clouds and therefore can not reproduce such cases overestimating LW_d and T_s. The third grey period is different caused by a shift in the position of a stormy intrusion relative to the grid cell of Polarstern.

The positive bias in LW_d leads to a positive bias in LW_net in the same time spans (Figure 6.2 and Table 4.1). This means the monthly positive bias of LW_d of $15.97\,\mathrm{Wm^{-2}}$ outweighs the monthly negative bias in LW_u of $-7.96\,\mathrm{Wm^{-2}}$ (Table 4.1).

To conclude, these results match the hypothesis that biases in cloud representation and in particular an overestimated LWP cause positive biases in LW_d, and thus lead to a warming and overestimated surface temperature. This occurs specifically during observed clear-sky, cold conditions.

Not only clouds influence the LW_d but also the amount of water vapour in the atmosphere [49]. Figure 4.4 shows the pdf plot of integrated water vapour (IWV) and liquid water path (LWP) for MOSAiC and HIRHAM-NAOSIM data. For IWV the graph of $CTRL$ is shifted towards smaller values with $MBE = -0.55\,\mathrm{kgm^{-2}}$ (Table 4.1), whereas the opposite is visible in the pdf plot of LWP with a monthly positive bias in February 2020 of $2.66\,\mathrm{gm^{-2}}$. The fact that the bias of LW_d is positive leads to the conclusion that the influence of the positive bias in LWP on LW_d is bigger than the negative bias in IWV.
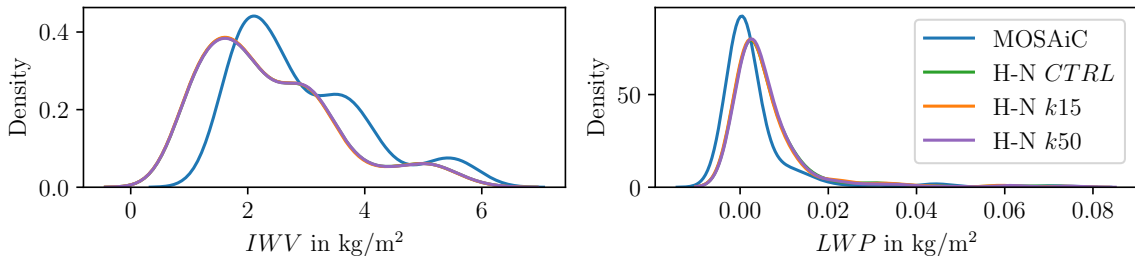

Figure 4.4: Plots of the pdf for integrated water vapour (IWV) on the left and liquid water path (LWP) on the right side for MOSAiC data (blue) and HIRHAM-NAOSIM's nearest grid cells to Met City and the ASFS. The plots are based on three-hourly data from February 2020. The $CTRL$ run is depicted in green, $k15$ in orange and $k50$ in purple.

Closely related to the evaluation of the longwave radiation and clouds is the representation of the two Arctic winter states (described in Section 2.1). For this, Figure 4.5 shows a bivariate histogram of LW_net and low-level stability ΔT [50]. The low-level stability is calculated as temperature difference between the temperature at $10\,\mathrm{m}$ height and at the surface. For calculating the relative frequency, model data are only used when there are also observational data available.

The cloudy state in the MOSAiC histogram (Figure 4.5, left) is associated with ΔT centered around $0\,\mathrm{K}$ and LW_net around $-15\,\mathrm{Wm^{-2}}$. The clear state has a maximum in relative frequency of occurrence for temperature differences at around $1.5\,\mathrm{K}$ and LW_net at approximately $-50\,\mathrm{Wm^{-2}}$. In other words, the two states can be detected as
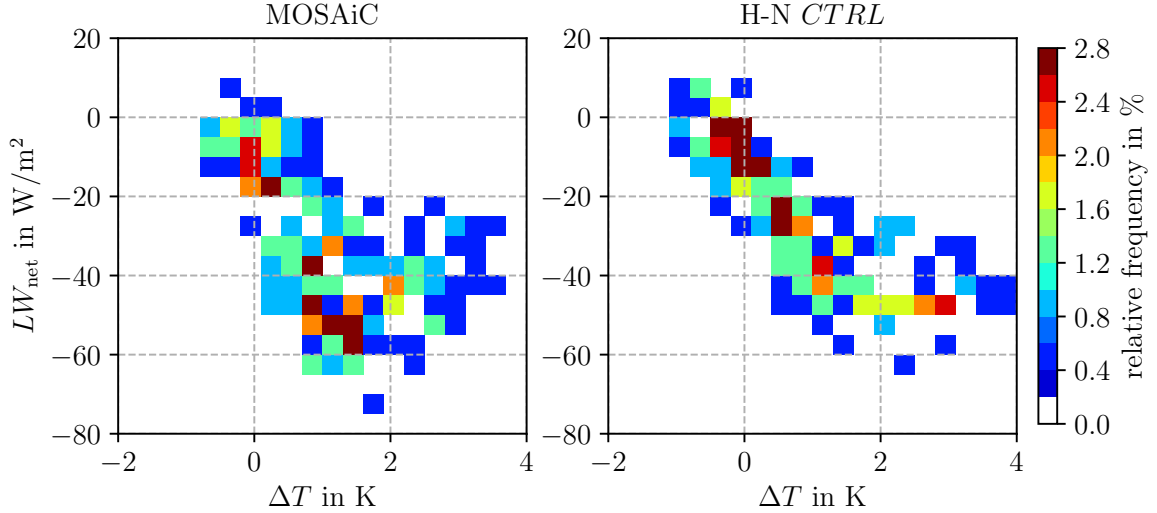
Figure 4.5: Two-dimensional histogram of LW_{net} over $\Delta T = T_{10m} - T_s$ for February 2020 based on three-hourly data from MOSAiC (left) and the model $CTRL$ run (right) at Met City.

bimodal distributions in LW_{net} and ΔT.

Compared to this, the relative frequency in the histogram of $CTRL$ (Figure 4.5, right) has a maximum for the cloudy state centered around $0\,K$ and $-10\,Wm^{-2}$ but there is an absence of the radiatively clear state. The cloudy state has a higher frequency of occurrence in the model $CTRL$ run than observed. This is reflected in the positive bias in LWP and LW_d.

4.1.3 Atmospheric Stability

The atmospheric stratification is closely related to the Arctic temperature inversion. If the simulated atmosphere is not stable enough, too much mixing results in insufficient cooling of the surface and overestimated surface temperatures.

As a measure for atmospheric stability, the bulk Richardson number Ri_B at the lowest model level at $10\,m$ height, calculated with Equation (2.3), is taken into account. A time series of Ri_B is shown in Figure 4.6. The observed Ri_B is based on the Met Tower temperatures. During stormy events (blue hatched periods), the observed Ri_B is generally lower than 0.02 and the atmospheric stability can be classified as neutral. The atmospheric stratification is especially neutral during the second blue time period when values of Ri_B are around zero. MOSAiC's Ri_B has peaks with values higher than 0.3 and around 0.15 in the first and third grey area. At these times, the atmosphere shows stable stratification. This is in accordance to the described cold, high-pressure situation. High numbers of Ri_B can be interpreted as stable conditions due to low wind speed conditions, potentially accompanied by a strong vertical temperature gradient.

The general occurrence of neutral and stable stratification associated with the different synoptic situations is reproduced by the models $CTRL$ run. During stormy events, the near zero Ri_B and neutral conditions are well simulated. The model shows an increased Ri_B and stable conditions during observed clear-sky cold periods but the stratification
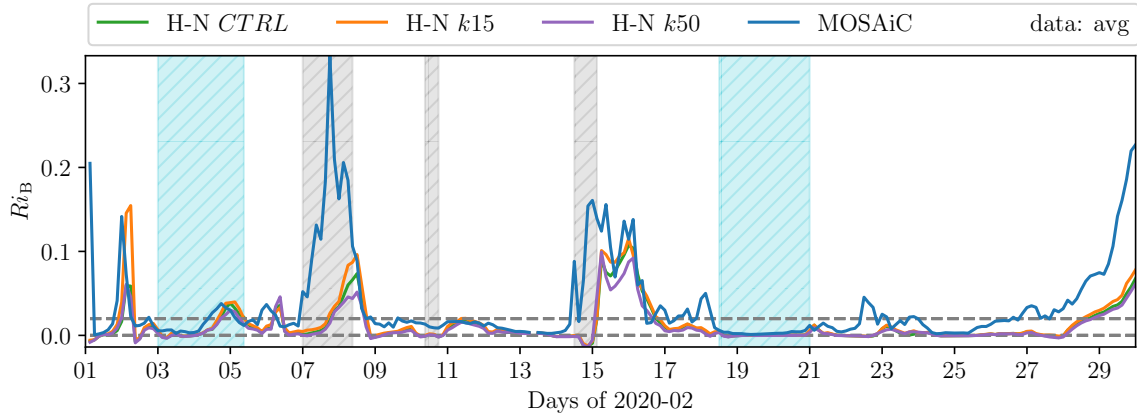
Figure 4.6: Time series of bulk Richardson number at $10\,\mathrm{m}$ height for three-hourly data from MOSAiC observations and HIRHAM-NAOSIM model runs at Met City. Dashed grey lines separate unstable ($Ri_\mathrm{B} < 0$), neutral and stable ($0.02 \leq Ri_\mathrm{B}$) stratification.

Table 4.2: Percentages of time steps with different stabilities of bulk Richardson number divided into three categories for February 2020. The frequency of occurrence is calculated for three-hourly data from HIRHAM-NAOSIM runs and MOSAiC data from Met City for Ri_B at $10\,\mathrm{m}$ height.

	unstable $Ri_\mathrm{B} < 0$ in %	neutral $0 \leq Ri_\mathrm{B} < 0.02$ in %	stable $0.02 \leq Ri_\mathrm{B}$ in %
MOSAiC	0	61	39
$CTRL$	27	56	17
$k15$	23	56	21
$k50$	29	54	17

is not as strong as observed.

As discussed before, the $CTRL$ run shows a different behaviour in the third grey time period, caused by a shift in the position of a storm event relative to the grid cell of Polarstern. Ri_B of $CTRL$ run decreases towards negative values connected with unstable atmospheric stratification while the observed atmosphere is stable.

A conclusion from Figure 4.6 is that in the stormy time periods (blue hatched) neutral and stable stratification is reproduced well by the $CTRL$ run. The model underestimates neutral and stable stratification during observed clear-sky cold times.

To statistically quantify the occurrence of different stabilities, Ri_B is classified in three categories (Table 4.2). The atmospheric stratification is considered unstable for negative values of Ri_B, neutral for $0 \leq Ri_\mathrm{B} < 0.02$, and stable for $0.02 \leq Ri_\mathrm{B}$ [10]. The results show that the $CTRL$ run overestimates unstable situations with a difference of $27\,\%$ and underestimates the occurrence of stable stratification by $22\,\%$.

For further examination of the overestimated unstable situations with negative Ri_B, the buoyancy and shear terms of Ri_B or in other words the denominator and numerator of Equation (2.3) are plotted separately as pdfs in Figure 4.7. The form of the model pdfs corresponds to the observed ones but there is a shift of approximately $0.5\,\mathrm{m^2 s^{-2}}$ in buoyancy towards lower values. The negative bias in Ri_B mainly results from this
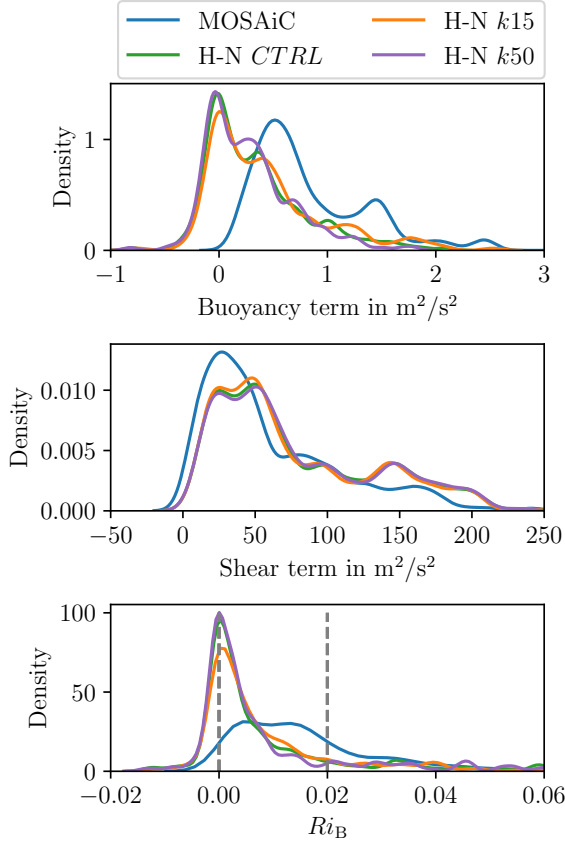
Figure 4.7: Plots of the pdf for the buoyancy term (top) and shear term (middle) of Ri_{B} as well as for the Ri_{B} (bottom). Three-hourly data from MOSAiC Met City (blue) and HIRHAM-NAOSIM model runs (green, orange, purple) are used. Grey dashed vertical lines in the plot of Ri_{B} mark limits of unstable ($Ri_{\mathrm{B}} < 0$), neutral and stable ($0.02 \leq Ri_{\mathrm{B}}$) stratification.

underestimation of the buoyancy term.

To conclude, the model underestimates the atmospheric stability during observed clear-sky, cold conditions caused by a negative bias in the buoyancy term. $CTRL$ also underestimates the occurrence of stable stratification. As a result, the simulated atmosphere during clear-sky events is mixed stronger than observed and the surface temperature of $CTRL$ has the positive bias discussed in Section 4.1.1. In addition to this result, it can be seen that the $CTRL$ run is able to reproduce neutral and stable stratification during stormy periods.

4.2 Impact of Changed Snow Thermal Conductivity

Changing the snow thermal conductivity k_{s} directly affects the conductive flux through the snow and as a result T_{s}, LW_{u} and the whole SEB. An inappropriate choice of a too high k_{s} can be the reason for an overestimated surface temperature.

Figure 4.8 shows time series of the differences ΔH_c (top) and ΔT_s (bottom) between $k15$ and $CTRL$ run at the nearest grid cell to Met City for February 2020. The thermal conductivity of snow in $k15$ is reduced by $0.16\,\mathrm{Wm^{-1}K^{-1}}$ compared to $CTRL$. A smaller snow thermal conductivity reduces the heat transfer through the snow layer, and the modeled H_{c} through sea ice and snow becomes smaller by $2\,\mathrm{Wm^{-2}}$ to $6\,\mathrm{Wm^{-2}}$.

In the blue hatched and the third grey stormy periods the H_{c} difference of $k15$ and $CTRL$ is smaller than in the rest of February. As a consequence of the reduced H_{c} in run $k15$, the surface temperature decreases as well, with a maximal difference to $CTRL$
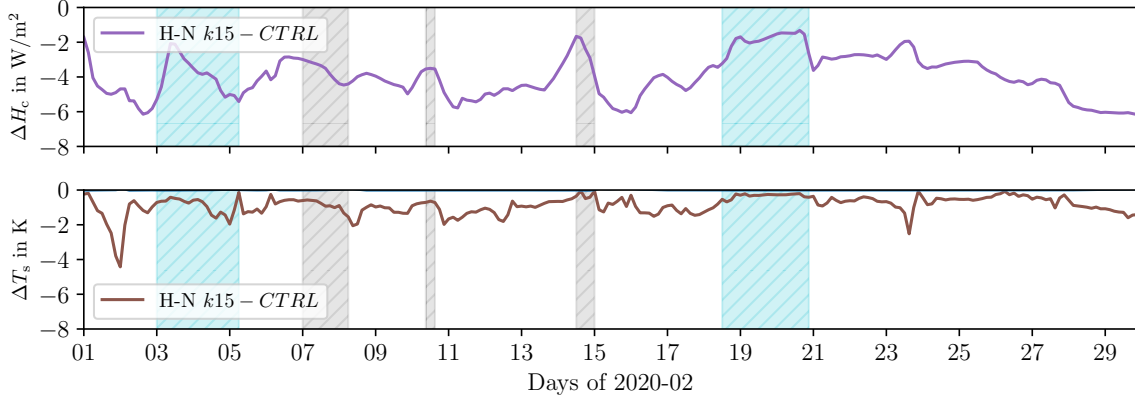
Figure 4.8: Time series of ΔH_c (top) and ΔT_s (bottom) as differences between $k15$ and $CTRL$. The model output is three-hourly data from the nearest grid cell to Met City in February 2020. Synoptic events are hatched in blue and grey.

of around $5\,\mathrm{K}$. The correlation between the time series of H_c and T_s is 0.46. In the second blue hatched time period, the temperature difference between $k15$ and $CTRL$ is near $0\,\mathrm{K}$. This contradicts the expected improvement when choosing a smaller k_s to simulate freshly fallen snow during storm events. In the first two grey periods, the surface temperature is slightly reduced by approximately $1\,\mathrm{K}$ to $2\,\mathrm{K}$.

Figure 4.1 and Figure 4.2 show a clear shift towards lower T_s with smaller k_s. Comparing the temperature MBE of $k15$ and $CTRL$ in Table 4.1 the monthly T_s bias is reduced by approximately $1\,\mathrm{K}$ (i.e. the MBE for $k15$ is $1.27\,\mathrm{K}$ and thus smaller compared to $CTRL$ which has a MBE of $2.13\,\mathrm{K}$). The $RMSE$ for T_s is smaller for $k15$ as well ($RMSE = 2.51\,\mathrm{K}$).

Because the liquid water path (LWP) of all model runs is similar, there are only small differences between the runs when it comes to LW_d (Figure 4.3). To evaluate the connection between the LW_d forcing (Section 4.1.2) and the change of k_s, the scatter plot in Figure 4.9 shows the conductive heat flux (H_c) over LW_d. A linear regression is

Figure 4.9: Scatterplot of conductive heat flux (H_c) over downward longwave radiation (LW_d) for three model runs with different k_s. A linear regression is plotted with its standard deviation with confidence interval of $68\,\%$.
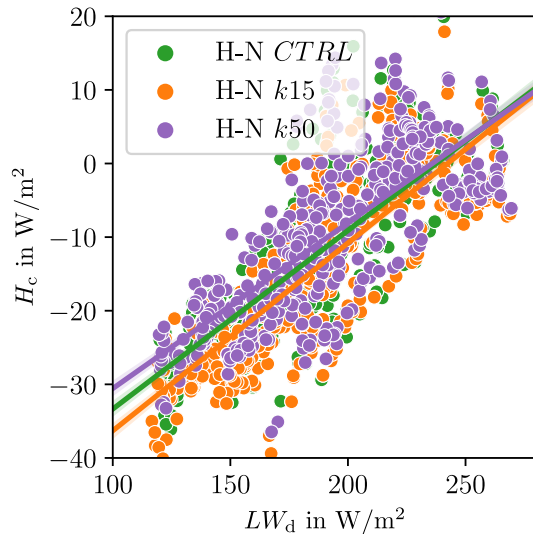
made with a confidence interval of $68\,\%$. At smaller LW_d in clear-sky conditions, the

impact of a changed k_s on H_c is more apparent due to a generally larger conductive flux through the ice surface. Therefore a change of k_s has a larger impact at times with clear-sky than in warmer, cloudier time periods. This becomes visible in the small values of ΔH_c in the blue hatched periods in Figure 4.8. Nevertheless, there are also minima in the amount of ΔH_c in the grey hatched periods caused by the positive LW_d bias during these times (Figure 4.3).

To conclude: Although the monthly T_s bias is reduced by lowering k_s, the pronounced positive temperature bias during cold, clear-sky periods remains. Changing k_s has the biggest impact on H_c and T_s in clear-sky time spans, but these are not well represented in the model.

A reduction in k_s and related cooler T_s are associated with according SEB changes. To demonstrate this, Figure 4.10 shows the pdf plots for SEB (left), LW_net (middle) and H_s (right) of the HIRHAM-NAOSIM model runs. The decrease in energy transport through the snow and resulting smaller surface temperature reduces the amount of LW_u according to the Stefan-Boltzmann law. The less negative LW_u causes a shift of LW_net pdf to the right (Figure 4.10, middle). This means the LW_net loss from the surface is smaller. The pdf of the sensible heat flux is also shifted to the right due to its linear relation to ΔT (Figure 4.10, right) and consequently SEB becomes less negative compared to MOSAiC data (Figure 4.10, left). These changes make the model biases larger. Table 4.1 gives quantitative information of the changed biases. The monthly MBE of LW_net increases by $1.45\,\mathrm{Wm^{-2}}$ and the MBE of H_s by $2.14\,\mathrm{Wm^{-2}}$ in $k15$ compared to $CTRL$. The $RMSE$ of SEB increases by $3.96\,\mathrm{Wm^{-2}}$ to $20.54\,\mathrm{Wm^{-2}}$ and $k15$ and MOSAiC data is less correlated for H_s and SEB.
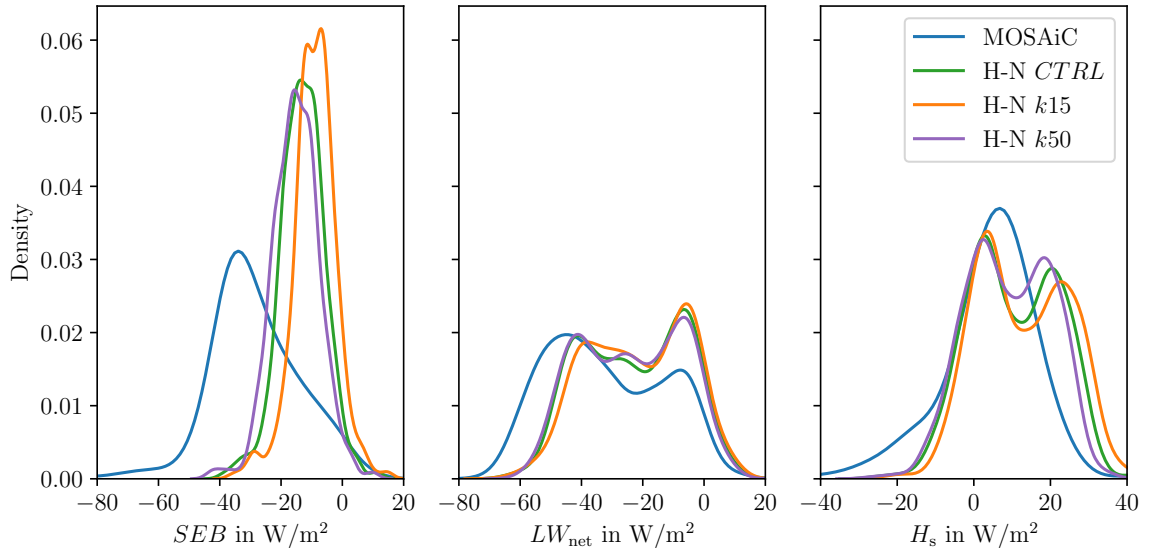

Figure 4.10: Plots of the pdf for SEB (left) and its main winter components LW_net (middle) and H_s (right). The plots are based on three-hourly data of MOSAiC observation and HIRHAM-NAOSIM values from the nearest grid cells to Met City and ASFS in February 2020.

A pdf plot of ΔT in Figure 4.11 depicts that a smaller k_s causes a broader range of the simulated ΔT compared to the temperature difference of MOSAiC data. In contrast to MOSAiC data, the temperature at $10\,\mathrm{m}$ height is more often below the surface temperature in HIRHAM-NAOSIM model runs. The temperature inversion is not simulated accurately.

Figure 4.11: Probability density function of $\Delta T = T_{10\mathrm{m}} - T_s$ for the model runs with different k_s (green, orange, purple) and MOSAiC data (blue). The data are three-hourly means of February 2020 from Met City and the ASFS as well as their nearest grid cells in HIRHAM-NAOSIM.
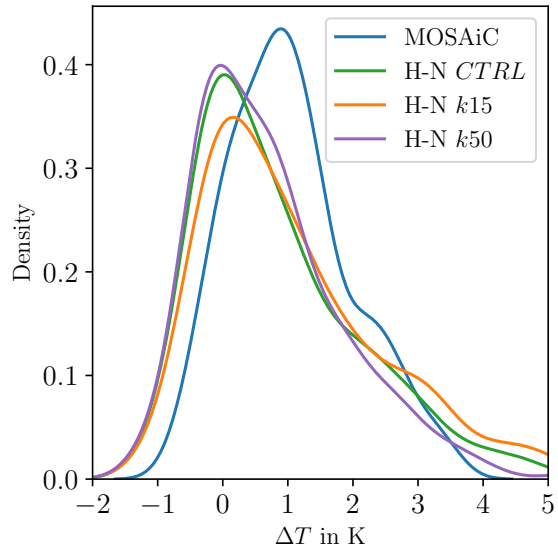

Figure 4.7 in Section 4.1.3 shows how the model reacts to a changed snow thermal conductivity concerning the atmospheric stability and stratification. The shear term depicted in the middle of the graphic hardly differs for the model runs. The buoyancy pdf of Ri_B from $k15$ is slightly denser at higher values. This is reflected in Figure 4.6. The Ri_B time series of $k15$ rises to higher values than the $CTRL$ run, especially in the end or shortly after the first and third grey hatched time span. HIRHAM-NAOSIM $k15$ is able to simulate the peak of Ri_B around 2020-02-02. Nevertheless, the underestimation of the occurrence of stable condition remains. As noted in Table 4.2, the percentage of stable conditions increases by $4\,\%$ up to $21\,\%$ for $k15$ but stays under the observed percentage of $39\,\%$ stable conditions. Unstable situations are still overestimated by $23\,\%$.

The height of the snow thermal conductivity is linked to other sea ice properties. A smaller conductive heat flux and energy transport through the snow at lower k_s insulates the ice from the colder atmosphere. As a result, the sea ice is warmer and there is less bottom sea ice growth. The opposite applies for higher k_s [12]. This effect can be seen in Figure 4.12. A difference of $\Delta k_s = 0.16\,\mathrm{Wm^{-1}K^{-1}}$ leads to a vertical ice growth of up to $\Delta h_i = 40\,\mathrm{cm}$ in central Arctic at Polarstern.

A changed k_s in the opposite direction towards the value of the MOSAiC expedition $k_s = 0.5\,\mathrm{Wm^{-1}K^{-1}}$ in $k50$ increases the surface temperature, compared to $CTRL$, as a result of a less insulating snow layer (Figure 4.1). The MBE of February rises to $2.56\,\mathrm{K}$. Figures 4.10 and 6.2 show the shift of SEB, LW_net and H_s towards less positive values above 0 and more negative values in the negative range especially for SEB (shifted to the left). The correlation between MOSAiC and HIRHAM-NAOSIM rises with the higher k_s for all components of SEB, and the surface temperature and the MBE of SEB is reduced.
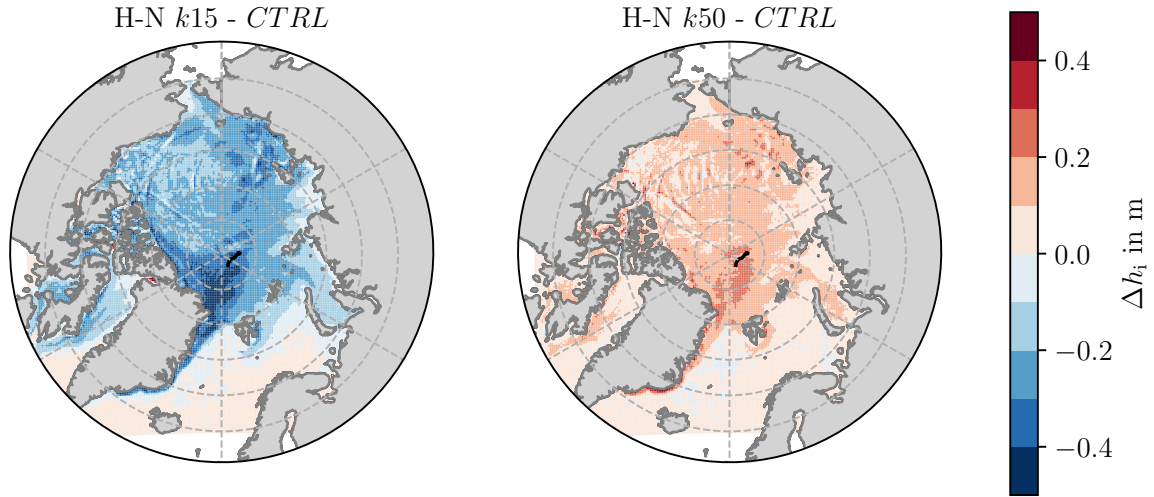
Figure 4.12: Spatial plots over central Arctic of monthly three-hourly mean of February ice thickness differences Δh_i between $k15$ and $CTRL$. The position of Met City is plotted for every day in February 2020.

Despite this, the lowered snow insulation effect causes more heat transfer through the snow and less atmospheric stability (Figure 4.6). The frequency of occurrence of unstable atmospheric stratification is overestimated by 29%, 2% more than by $CTRL$.

5 Summary and Outlook

The coupled Arctic atmosphere-ocean-sea ice model HIRHAM-NAOSIM is evaluated compared to data from the MOSAiC expedition for Arctic wintertime. February 2020 is chosen for the comparison, and five synoptic periods including the radiatively clear and opaquely cloudy state are specifically considered.

The analysis shows that HIRHAM-NAOSIM's control run ($CTRL$) is able to simulate temporal changes of the surface temperatures at Polarstern with a high correlation of 0.89. Especially during cyclone events and moisture intrusions with a low atmospheric stability, the surface temperature as well as the components of the surface energy budget are in good agreement with MOSAiC observations. The radiative components of the surface energy budget (SEB) are higher correlated to MOSAiC data than the non-radiative sensible heat flux.

In addition to a general evaluation, the focus of the analysis lies on HIRHAM-NAOSIM's positive temperature bias especially during clear-sky conditions. The control run $CTRL$ underestimates the occurrence of the clear-sky state, but overestimates the liquid water path (LWP) in clear-sky, cold conditions causing a positive bias of longwave radiation directed towards the surface (LW_d). Additionally, the frequency of occurrence of the cloudy state is higher than observed. The evaluation shows that the model underestimates the occurrence of stable conditions due to a negative bias in the buoyancy term of the bulk Richardson number (Ri_B). Atmospheric layers are less stable and the temperature inversion is less pronounced. Whether the stratification bias is a consequence of the LW_d bias cannot be ruled out.

A reduced snow thermal conductivity (k_s) of $0.15\,\mathrm{Wm^{-1}K^{-1}}$ causes a decrease of the monthly $CTRL$ temperature bias, but the surface temperature (T_s) during cold temperature periods remains too high. The warming effect of the positive cloud bias outweighs the surface cooling which results from the change towards a smaller snow thermal conductivity. During clear-sky conditions, a change of k_s has a bigger impact on the conductive heat flux (H_c) and thus on the surface temperature. Due to the underestimation of stable conditions, the model overestimates LWP and LW_d in the same time periods. As a result, the changed k_s can not reduce the surface temperature as much as needed. The suggested higher snow thermal conductivity of MOSAiC expedition $k_\mathrm{s} = 0.50\,\mathrm{Wm^{-1}K^{-1}}$ leads to an increased correlation between HIRHAM-NAOSIM $k50$ and MOSAiC data, compared to $CTRL$. The monthly positive SEB bias is reduced but the negative temperature bias at colder times is enhanced. Due to the heterogeneous surface of the Arctic sea ice one constant parameter of k_s can not represent the observed situation. Nevertheless, the snow thermal conductivity can be one factor when adjusting HIRHAM-NAOSIM's atmospheric stability towards a more stable stratification, as the occurrence of stable conditions increases by $4\,\%$ when reducing k_s by $0.16\,\mathrm{Wm^{-1}K^{-1}}$.

A challenge of the evaluation of the Arctic climate model to MOSAiC data is the

comparison of an averaged grid cell to stations. Most of the time there are no big differences between neighbouring grid cells of HIRHAM-NAOSIM over sea ice, but especially when the Polarstern is nearby a stormy event, more than one grid cell of the model should be taken into account.

One-at-a-time sensitivity analyses, as carried out by changing only the snow thermal conductivity and comparing the modified runs of HIRHAM-NAOSIM to the control run $CTRL$, help to get an impression of how the model reacts to the change in single parameters. Besides this, it is important to gain a better understanding of the interactions between climate variables and feedback linkages of climate models in analyses concerning all input parameters and their biggest uncertainties in the used climate model [12].

As investigated by Schneider et al. [10] for the stand-alone model HIRHAM5, the coupled model HIRHAM-NAOSIM also has a deficit in simulating atmospheric stability during Arctic winter clear-sky events. Closely related to the atmospheric stratification, the temperature inversion is an important Arctic winter characteristic [51] and its representation in HIRHAM-NAOSIM must be improved.

Bibliography

[1] C. Hirt, S. Claessens, T. Fecher, *et al.*, "New ultrahigh-resolution picture of Earth's gravity field," *Geophysical Research Letters*, vol. 40, no. 16, pp. 4279–4283, 2013, ISSN: 1944-8007. DOI: 10.1002/grl.50838.

[2] B. Klose, *Meteorologie: Eine interdisziplinäre Einführung in die Physik der Atmosphäre*. Berlin, Heidelberg: Springer Berlin Heidelberg, 2008, ISBN: 978-3-540-71308-1. DOI: 10.1007/978-3-540-71309-8.

[3] Intergovernmental Panel on Climate Change (IPCC), *Climate Change 2022: Impacts, Adaptation, and Vulnerability*, H.-O. Pörtner, D. Roberts, M. Tignor, *et al.*, Eds. Cambridge University Press, 2022.

[4] M. Meredith, M. Sommerkorn, S. Cassotta, *et al.*, "Polar Regions," in *IPCC Special Report on the Ocean and Cryosphere in a Changing Climate*, Cambridge University Press, 2022, pp. 203–320. DOI: 10.1017/9781009157964.005.

[5] M. Serreze and J. Francis, "The arctic amplification debate," *Climatic Change*, vol. 76, pp. 241–264, Jun. 2006. DOI: 10.1007/s10584-005-9017-y.

[6] J. C. Stroeve, V. Kattsov, A. Barrett, *et al.*, "Trends in Arctic sea ice extent from CMIP5, CMIP3 and observations," *Geophysical Research Letters*, vol. 39, no. 16, 2012, ISSN: 1944-8007. DOI: 10.1029/2012GL052676.

[7] M. D. Shupe, M. Rex, K. Dethloff, *et al.*, "Arctic report card 2020: The MOSAiC expedition: A year drifting with the arctic sea ice," 2020. DOI: 10.25923/9G3V-XH92.

[8] W. Dorn, A. Rinke, C. Köberle, *et al.*, "Evaluation of the sea-ice simulation in the upgraded version of the coupled regional atmosphere-ocean- sea ice model HIRHAM–NAOSIM 2.0," *Atmosphere*, vol. 10, no. 8, p. 431, 2019, ISSN: 2073-4433. DOI: 10.3390/atmos10080431.

[9] Y. Batrak and M. Müller, "On the warm bias in atmospheric reanalyses induced by the missing snow over arctic sea-ice," *Nature Communications*, vol. 10, no. 1, p. 4170, 2019, ISSN: 2041-1723. DOI: 10.1038/s41467-019-11975-3.

[10] T. Schneider, C. Lüpkes, W. Dorn, *et al.*, "Sensitivity to changes in the surface-layer turbulence parameterization for stable conditions in winter: A case study with a regional climate model over the arctic," *Atmospheric Science Letters*, vol. 23, no. 1, e1066, 2022, ISSN: 1530-261X. DOI: 10.1002/asl.1066.

[11] D. Barber, K. Dethloff, S. Gerland, *et al.*, "MOSAiC- multidisciplinary drifting observatory for the study of arctic climate - science plan," 2016.

[12] J. R. Urrego-Blanco, N. M. Urban, E. C. Hunke, *et al.*, "Uncertainty quantification and global sensitivity analysis of the los alamos sea ice model," *Journal of Geophysical Research: Oceans*, vol. 121, no. 4, pp. 2709–2732, 2016, ISSN: 2169-9291. DOI: 10.1002/2015JC011558.

[13] M. C. Serreze and R. G. Barry, *The Arctic climate system*, Second edition, ser. Cambridge atmospheric and space science series. New York, USA: Cambridge University Press, 2014.

[14] O. Lecomte, T. Fichefet, M. Vancoppenolle, *et al.*, "On the formulation of snow thermal conductivity in large-scale sea ice models," *Journal of Advances in Modeling Earth Systems*, vol. 5, no. 3, pp. 542–557, 2013, ISSN: 19422466. DOI: 10.1002/jame.20039.

[15] M. Nicolaus, D. K. Perovich, G. Spreen, *et al.*, "Overview of the MOSAiC expedition: Snow and sea ice," *Elementa: Science of the Anthropocene*, vol. 10, no. 1, p. 000 046, 2022, ISSN: 2325-1026. DOI: 10.1525/elementa.2021.000046.

[16] M. D. Shupe and J. M. Intrieri, "Cloud radiative forcing of the arctic surface: The influence of cloud properties, surface albedo, and solar zenith angle," *Journal of Climate*, vol. 17, no. 3, pp. 616–628, 2004, ISSN: 0894-8755, 1520-0442. DOI: 10.1175/1520-0442(2004)017<0616:CRFOTA>2.0.CO;2.

[17] M. Kayser, M. Maturilli, R. M. Graham, *et al.*, "Vertical thermodynamic structure of the troposphere during the norwegian young sea ICE expedition (n-ICE2015)," *Journal of Geophysical Research: Atmospheres*, vol. 122, no. 20, pp. 10, 855–10, 872, 2017, ISSN: 2169-8996. DOI: 10.1002/2016JD026089.

[18] K. Stramler, A. D. D. Genio, and W. B. Rossow, "Synoptically driven arctic winter states," *Journal of Climate*, vol. 24, no. 6, pp. 1747–1762, 2011. DOI: 10.1175/2010JCLI3817.1.

[19] R. M. Graham, A. Rinke, L. Cohen, *et al.*, "A comparison of the two arctic atmospheric winter states observed during n-ICE2015 and SHEBA," *Journal of Geophysical Research: Atmospheres*, vol. 122, no. 11, pp. 5716–5737, 2017, ISSN: 2169-8996. DOI: 10.1002/2016JD025475.

[20] L. Cohen, S. R. Hudson, V. P. Walden, *et al.*, "Meteorological conditions in a thinner arctic sea ice regime from winter to summer during the norwegian young sea ice expedition (n-ICE2015)," *Journal of Geophysical Research: Atmospheres*, vol. 122, no. 14, pp. 7235–7259, 2017, ISSN: 2169-8996. DOI: 10.1002/2016JD026034.

[21] A. S. Monin and A. M. Obukhov, "Basic laws of turbulent mixing in the surface layer of the atmosphere," *Tr. Akad. Nauk SSSR Geophiz. Inst.*, no. 24, pp. 163–187, 1954.

[22] A. A. Grachev, E. L. Andreas, C. W. Fairall, *et al.*, "The critical richardson number and limits of applicability of local similarity theory in the stable boundary layer," *Boundary-Layer Meteorology*, vol. 147, no. 1, pp. 51–82, 2013, ISSN: 0006-8314, 1573-1472. DOI: 10.1007/s10546-012-9771-0.

[23] M. Webster, S. Gerland, M. Holland, *et al.*, "Snow in the changing sea-ice systems," *Nature Climate Change*, vol. 8, no. 11, pp. 946–953, 2018, ISSN: 1758-6798. DOI: 10.1038/s41558-018-0286-7.

[24] M. Sturm, J. Holmgren, M. König, *et al.*, "The thermal conductivity of seasonal snow," *Journal of Glaciology*, vol. 43, no. 143, pp. 26–41, 1997, ISSN: 0022-1430, 1727-5652. DOI: 10.3189/S0022143000002781.

[25] M. Sturm, "Thermal conductivity and heat transfer through the snow on the ice of the beaufort sea," *Journal of Geophysical Research*, vol. 107, p. 8043, C10 2002, ISSN: 0148-0227. DOI: 10.1029/2000JC000409.

[26] W. Dorn, K. Dethloff, and A. Rinke, "Improved simulation of feedbacks between atmosphere and sea ice over the arctic ocean in a coupled regional climate model," *Ocean Modelling*, vol. 29, no. 2, pp. 103–114, 2009, ISSN: 1463-5003. DOI: `10.1016/j.ocemod.2009.03.010`.

[27] F. Riche and M. Schneebeli, "Thermal conductivity of snow measured by three independent methods and anisotropy considerations," *The Cryosphere*, vol. 7, no. 1, pp. 217–227, 2013, ISSN: 1994-0424. DOI: `10.5194/tc-7-217-2013`.

[28] T. Fichefet, B. Tartinville, and H. Goosse, "Sensitivity of the antarctic sea ice to the thermal conductivity of snow," *Geophysical Research Letters*, vol. 27, no. 3, pp. 401–404, 2000, ISSN: 1944-8007. DOI: `10.1029/1999GL002397`.

[29] W. W. Kellogg and S. H. Schneider, "Climate stabilization: For better or for worse?: Even if we could predict the future of our climate, climate control would be a hazardous venture.," *Science*, vol. 186, no. 4170, pp. 1163–1172, 1974, ISSN: 0036-8075, 1095-9203. DOI: `10.1126/science.186.4170.1163`.

[30] "The expedition: An entire year trapped in the ice," MOSAiC Expedition. (2019), [Online]. Available: `https://mosaic-expedition.org/expedition/` (visited on 06/26/2022).

[31] M. D. Shupe, M. Rex, B. Blomquist, *et al.*, "Overview of the MOSAiC expedition: Atmosphere," *Elementa: Science of the Anthropocene*, vol. 10, no. 1, p. 00 060, 2022, ISSN: 2325-1026. DOI: `10.1525/elementa.2021.00060`.

[32] K. Ebell, A. Walbröl, R. Engelmann, *et al.*, "Temperature and humidity profiles, integrated water vapour and liquid water path derived from the HATPRO microwave radiometer onboard the polarstern during the MOSAiC expedition," 2022. DOI: `10.1594/PANGAEA.941389`.

[33] P. O. G. Persson, C. W. Fairall, E. L. Andreas, *et al.*, "Measurements near the atmospheric surface flux group tower at SHEBA: Near-surface conditions and surface energy budget," *Journal of Geophysical Research: Oceans*, vol. 107, C10 2002, ISSN: 2156-2202. DOI: `10.1029/2000JC000705`.

[34] C. Köberle and R. Gerdes, "Simulated variability of the arctic ocean freshwater balance 1948–2001," *Journal of Physical Oceanography*, vol. 37, no. 6, pp. 1628–1644, 2007, ISSN: 0022-3670, 1520-0485. DOI: `10.1175/JPO3063.1`.

[35] J. H. Christensen, O. Christensen, P. Lopez, *et al.*, "The HIRHAM4 regional atmospheric climate model," *DMI Sci. Rep.*, vol. 96, no. 4, 51 pp. 1996.

[36] K. Dethloff, A. Rinke, R. Lehmann, *et al.*, "Regional climate model of the arctic atmosphere," *Journal of Geophysical Research: Atmospheres*, vol. 101, pp. 23 401–23 422, 1996, ISSN: 2156-2202. DOI: `10.1029/96JD02016`.

[37] A. Rinke, R. Gerdes, K. Dethloff, *et al.*, "A case study of the anomalous arctic sea ice conditions during 1990: Insights from coupled and uncoupled regional climate model simulations," *Journal of Geophysical Research: Atmospheres*, vol. 108, D9 2003, ISSN: 01480227. DOI: `10.1029/2002JD003146`.

[38] W. Dorn, K. Dethloff, A. Rinke, *et al.*, "Sensitivities and uncertainties in a coupled regional atmosphere-ocean-ice model with respect to the simulation of arctic sea ice," *Journal of Geophysical Research: Atmospheres*, vol. 112, D10 2007, ISSN: 01480227. DOI: `10.1029/2006JD007814`.

[39] M. Hanke, R. Redler, T. Holfeld, *et al.*, "YAC 1.2.0: New aspects for coupling software in earth system modelling," *Geoscientific Model Development*, vol. 9, no. 8, pp. 2755–2769, 2016, ISSN: 1991-959X. DOI: `10.5194/gmd-9-2755-2016`.

[40] H. Hersbach, B. Bell, P. Berrisford, *et al.*, "The ERA5 global reanalysis," *Quarterly Journal of the Royal Meteorological Society*, vol. 146, no. 730, pp. 1999–2049, 2020, ISSN: 1477-870X. DOI: `10.1002/qj.3803`.

[41] "Nudging-UKCA." (2018), [Online]. Available: `https://www.ukca.ac.uk/wiki/index.php/Nudging` (visited on 07/28/2022).

[42] M. Shupe, personal communication.

[43] "Synoptic - glossary of meteorology." (2012), [Online]. Available: `https://glossary.ametsoc.org/wiki/Synoptic` (visited on 07/26/2022).

[44] "Synoptic weather observation - glossary of meteorology." (2012), [Online]. Available: `https://glossary.ametsoc.org/wiki/Synoptic_weather_observation` (visited on 07/26/2022).

[45] "Scipy.spatial.cKDTree — SciPy v1.8.1 manual." (2008–2022), [Online]. Available: `https://docs.scipy.org/doc/scipy/reference/generated/scipy.spatial.cKDTree.html` (visited on 06/20/2022).

[46] "Seaborn.kdeplot — seaborn 0.11.2 documentation." (2012–2021), [Online]. Available: `https://seaborn.pydata.org/generated/seaborn.kdeplot.html` (visited on 06/20/2022).

[47] "Numpy.corrcoef — NumPy v1.22 manual." (2008–2022), [Online]. Available: `https://numpy.org/doc/stable/reference/generated/numpy.corrcoef.html` (visited on 06/20/2022).

[48] N. Henze, *Kovarianz und Korrelation*. Wiesbaden: Springer Fachmedien Wiesbaden, 2013, pp. 167–179, ISBN: 978-3-658-03077-3. DOI: `10.1007/978-3-658-03077-3_21`.

[49] J. G. Doyle, G. Lesins, C. P. Thackray, *et al.*, "Water vapor intrusions into the high arctic during winter," *Geophysical Research Letters*, vol. 38, no. 12, 2011. DOI: `https://doi.org/10.1029/2011GL047493`.

[50] F. Pithan, A. Ackerman, W. M. Angevine, *et al.*, "Select strengths and biases of models in representing the arctic winter boundary layer over sea ice: The larcform 1 single column model intercomparison," *Journal of Advances in Modeling Earth Systems*, vol. 8, no. 3, pp. 1345–1357, 2016, ISSN: 1942-2466. DOI: `10.1002/2016MS000630`.

[51] R. Bintanja, E. C. van der Linden, and W. Hazeleger, "Boundary layer stability and arctic climate change: A feedback study using EC-earth," *Climate Dynamics*, vol. 39, no. 11, pp. 2659–2673, 2012, ISSN: 1432-0894. DOI: `10.1007/s00382-011-1272-1`.
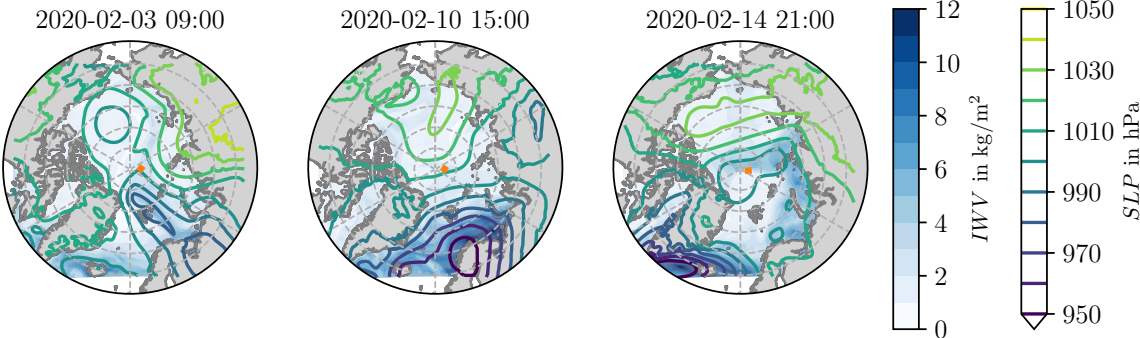
6 Appendix

Figure 6.1: Spatial plots of IWV (shaded) with isobares of SLP of $CTRL$ run for the central Arctic. The plots are based on three-hourly data for 2020-02-03 09:00 (left), 2020-02-10 15:00 (middle) and 2020-02-14 21:00 (right). The position of Met City is highlighted in orange.
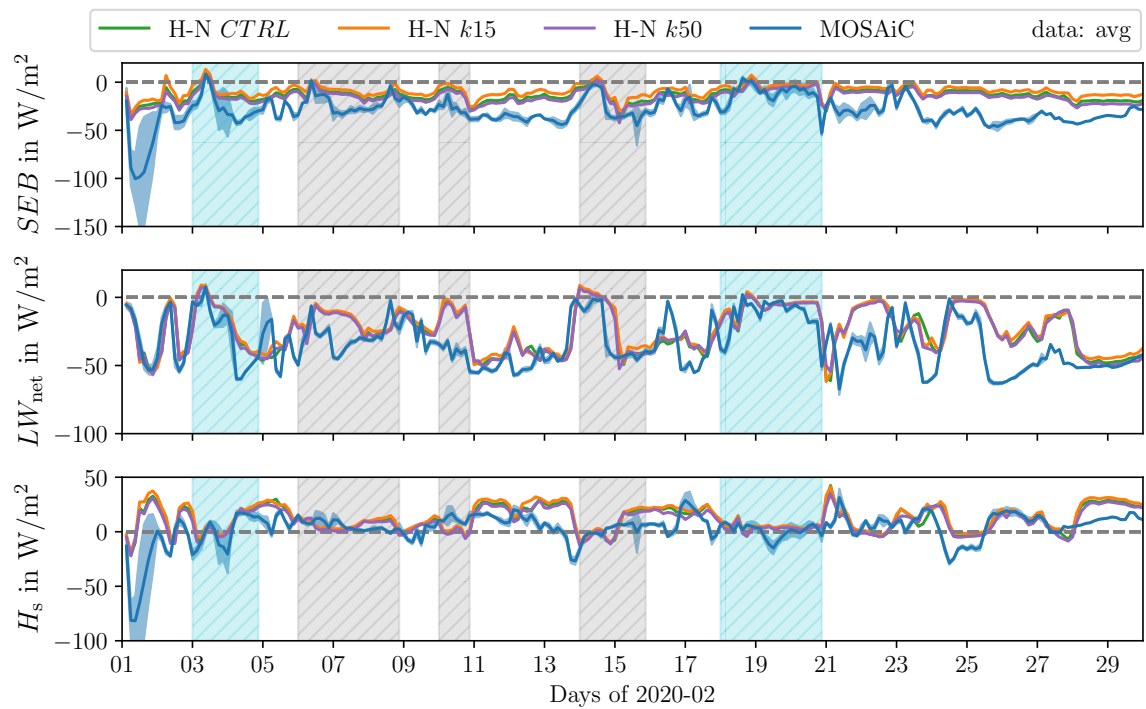
Figure 6.2: February 2020 time series of three-hourly data from MOSAiC (blue) and three model runs of HIRHAM-NAOSIM with different snow thermal conductivities in green, orange and purple at Met City and ASFS. SEB is plotted in the top plot, in the middle LW_{net} is depicted and the bottom plot shows H_{s}. The across station standard derivation of the MOSAiC data is plotted in blue as well.